The Astrophysical Journal Letters, 854:L24 (7pp), 2018 February 20 https://doi.org/10.3847/2041-8213/aaacfa

Ionized and Molecular Gas Kinematics in a $z = 1.4$ Star-forming Galaxy*

H. Übler[1], R. Genzel[1,2], L. J. Tacconi[1], N. M. Förster Schreiber[1], R. Neri[3], A. Contursi[1], S. Belli[1], E. J. Nelson[1], P. Lang[4], T. T. Shimizu[1], R. Davies[1], R. Herrera-Camus[1], D. Lutz[1], P. M. Plewa[1], S. H. Price[1], K. Schuster[3], A. Sternberg[5,6], K. Tadaki[7], E. Wisnioski[8], and S. Wuyts[9]
[1] Max-Planck-Institut für extraterrestrische Physik, Gießenbachstr. 1, D-85748 Garching, Germany; hannah@mpe.mpg.de
[2] Departments of Physics and Astronomy, University of California, Berkeley, CA 94720, USA
[3] Institut de Radioastronomie Millimétrique, 300 rue de la Piscine, F-38406 Saint Martin d'Hères, France
[4] Max-Planck-Institut für Astronomie, Königstuhl 17, D-69117 Heidelberg, Germany
[5] Raymond & Beverly Sackler School of Physics & Astronomy, Tel Aviv University, Ramat Aviv 69978, Israel
[6] Center for Computational Astrophysics, Flatiron Institute, 162 Fifth Avenue, New York, NY 10010, USA
[7] National Astronomical Observatory of Japan, 2-21-1 Osawa, Mitaka, Tokyo 181–8588, Japan
[8] Research School of Astronomy & Astrophysics, Australian National University, Canberra, ACT-2611, Australia
[9] Department of Physics, University of Bath, Claverton Down, Bath BA2 7AY, UK
Received 2017 December 12; revised 2018 February 3; accepted 2018 February 4; published 2018 February 16

Abstract

We present deep observations of a $z = 1.4$ massive, star-forming galaxy (SFG) in molecular and ionized gas at comparable spatial resolution (CO 3–2, NOrthern Extended Millimeter Array (NOEMA); Hα, Large Binocular Telescope (LBT)). The kinematic tracers agree well, indicating that both gas phases are subject to the same gravitational potential and physical processes affecting the gas dynamics. We combine the one-dimensional velocity and velocity dispersion profiles in CO and Hα to forward-model the galaxy in a Bayesian framework, combining a thick exponential disk, a bulge, and a dark matter halo. We determine the dynamical support due to baryons and dark matter, and find a dark matter fraction within one effective radius of $f_{\rm DM}(\leqslant R_e) = 0.18^{+0.06}_{-0.04}$. Our result strengthens the evidence for strong baryon-dominance on galactic scales of massive $z \sim 1$–3 SFGs recently found based on ionized gas kinematics alone.

Key words: galaxies: evolution – galaxies: high-redshift – galaxies: kinematics and dynamics

1. Introduction

Our knowledge of the kinematics of star-forming galaxies (SFGs) at $z = 1$–3 is dominated by large surveys targeting ionized gas emission (e.g., Förster Schreiber et al. 2009; Kriek et al. 2015; Wisnioski et al. 2015; Stott et al. 2016; Turner et al. 2017). There is strong evidence that the ionized gas kinematics of massive, high-redshift SFGs are dominated by ordered disk rotation, but a key question remains: how do the ionized gas kinematics, particularly the rotation curve and intrinsic velocity dispersion, compare to that of neutral or molecular gas, which dominate the gas mass budget?

Multiphase, spatially resolved data exist only for a handful of high-redshift SFGs, where the kinematics of the different gas phases are found to agree (e.g., Chen et al. 2017) or not (e.g., Swinbank et al. 2011 versus Olivares et al. 2016). Yet, deeper data are generally needed for at least one of the gas phases in these studies in order to compare the kinematics in detail, and to disentangle the contributions from baryons and dark matter. Genzel et al. (2013) showed through deep integrations of a $z = 1.5$ galaxy that its kinematics in Hα and CO(3–2) agree. However, this galaxy is undergoing a minor merger and is therefore not optimally suited to kinematically analyze the galaxy's baryon versus dark matter content.

In this Letter, we analyze the Hα and CO(3–2) kinematics of a massive SFG at $z = 1.4$, EGS4-24985. We have obtained deep data, 21 and 45 hr on source, with the Large Binocular Telescope (LBT) and the NOrthern Extended Millimeter Array (NOEMA), making this an unprecedented data set of two important tracers of the gas kinematics in an SFG. We model the galaxy by combining a thick exponential disk, a bulge, and an NFW (Navarro et al. 1996) halo, using Markov chain Monte Carlo (MCMC) sampling. We discuss correlations among the model parameters and constrain the galaxy's dark matter fraction within one effective radius (R_e). Throughout, we adopt a Chabrier (2003) initial mass function and a flat ΛCDM cosmology with $H_0 = 70\,{\rm km\,s^{-1}\,Mpc^{-1}}$, $\Omega_\Lambda = 0.7$, and $\Omega_m = 0.3$.

2. Data

2.1. Physical Properties of EGS4-24985

EGS4-24985 (R.A. $14^{\rm h}19^{\rm m}26\overset{\rm s}{.}66$, decl. $+52°51'17\overset{''}{.}0$) is a $z = 1.4$ galaxy with a stellar mass of $M_\star = 7.4 \times 10^{10} M_\odot$ and a star formation rate of ${\rm SFR} = 98.8\,M_\odot\,{\rm yr^{-1}}$ (both derived following the techniques outlined by Wuyts et al. 2011), placing it in the upper half of the main sequence at this redshift (Whitaker et al. 2014). The *V*-, *I*-, *H*-band ACS and WFC3 images reveal strong spatial color variations, indicative of a mixture of stellar populations, or varying dust obscuration that potentially hides a central mass concentration (Figure 1, left).

The morphological position angle ${\rm PA}_H = 18°$, minor-to-major axis ratio $q_H = 0.60$, $R_{e,H} = 0\overset{''}{.}52 = 4.4$ kpc, and Sérsic index $n_{S,H} = 0.74$ are constrained from GALFIT (Peng

* Based on observations carried out with the IRAM Interferometer NOEMA. IRAM is supported by INSU/CNRS (France), MPG (Germany), and IGN (Spain). Based on observations carried out with the LBT. The LBT is an international collaboration among institutions in the United States, Italy, and Germany. LBT Corporation partners are: LBT Beteiligungsgesellschaft, Germany, representing the Max-Planck Society, The Leibniz Institute for Astrophysics Potsdam, and Heidelberg University; The University of Arizona on behalf of the Arizona Board of Regents; Istituto Nazionale di Astrofisica, Italy; The Ohio State University, and The Research Corporation, on behalf of The University of Notre Dame, University of Minnesota and University of Virginia.

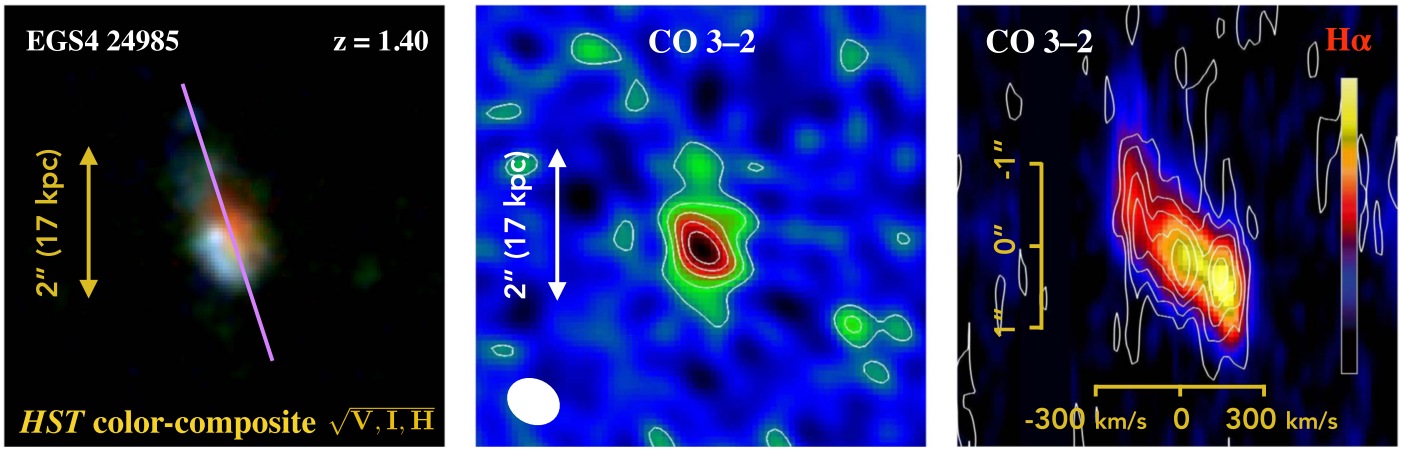

Figure 1. Left: *HST* color-composite image of EGS4-24985. The magenta line shows the morphological position angle. Middle: uniformly weighted CO(3–2) image. The white ellipse shows the clean beam. Right: Hα (intensity color scale) and CO (white intensity contours) position–velocity (PV) diagram.

et al. 2010) Sérsic models based on the 3D-*HST* team (Skelton et al. 2014) version of CANDELS *H*-band (F160W) imaging (Grogin et al. 2011; Koekemoer et al. 2011), presented by van der Wel et al. (2012). Assuming a ratio of scale height to scale length of $q_0 = 0.2$, typical for SFGs at this redshift (e.g., van der Wel et al. 2014), the estimated inclination is $i = 55°$. There is a systematic change in q as derived from other filters, $q = 0.54$–0.66 from F125W (*J*-band) to F814W (*I*-band).

Assuming a bulge-to-disk decomposition with $n_{S,\mathrm{disk}} = 1$, $n_{S,\mathrm{bulge}} = 4$, we infer the bulge-to-total fraction from the stellar mass map to be $B/T = 0.13 \pm 0.15$ (Lang et al. 2014).

2.2. CO Observations with NOEMA

To explore the kinematics of the cold gas, we observed the CO(3–2) line with the IRAM interferometer NOEMA. At the redshift of the source, the CO(3–2) line (rest frequency 345.796 GHz) is shifted into the 2 mm band. We observed EGS4-24985 in the D (compact) and A (extended) configurations with seven or eight antennas between 2016 November and 2017 April. The total equivalent eight-antenna on-source integration time was 45 hr in the D+A configuration, with a resolution of $0\farcs6$–$1\farcs0$. Weather conditions during the observing periods were excellent, with typical system temperatures of ~150 K. The WiDEX spectral correlator provided 4 GHz of bandwidth per polarization, with a fixed channel spacing of 2 MHz. For phase and amplitude calibration, every 20 minutes we alternated source observations with observations of a bright quasar within 15° of the source. The absolute flux calibration was done through bootstrapping from observations of LkHA-101 and MWC-349 (0.36 Jy and 1.45 Jy at 144 GHz), resulting in a continuum flux of 70 μJy.

The data were calibrated using the CLIC package of the IRAM GILDAS[10] software environment, and imaged and analyzed with the MAPPING routines in GILDAS. We applied a uniform weighting scheme to create the data cube, and then subtracted the 2 mm continuum emission using channels free of line emission. The final cube was CLEANED with the CLARK version of CLEAN implemented in GILDAS, and reconstructed with a $0\farcs67 \times 0\farcs55$ (PA = 62°) clean beam (Figure 1, middle), to a spectral resolution of 19 km s^{-1} with an rms noise of 0.2 mJy channel^{-1} synthesized beam^{-1}.

[10] http://www.iram.fr/IRAMFR/GILDAS

The molecular gas mass as measured from the CO(3–2) flux and using the α(CO) conversion function by Genzel et al. (2015) is $M_{\mathrm{mol}} = 6.9 \times 10^{10} M_{\odot}$. With a gas-to-baryonic mass fraction of $M_{\mathrm{mol}}/M_{\mathrm{bar}} = 0.48$, the galaxy is typical when compared to larger samples at the same redshift (Tacconi et al. 2018). The CO distribution has an approximate extent of $R_{e,\mathrm{CO}} \approx 0\farcs26$ (measured from an exponential disk fit in the UV plane). The CO position–velocity (PV) diagram is shown in Figure 1 (right, white contours).

2.3. Hα Observations with LUCI at LBT

We obtained seeing-limited near-infrared spectroscopy of EGS4-24985 using the LUCI1 and LUCI2 spectrographs in binocular mode (Buschkamp et al. 2012), mounted at the Bent Gregorian focus of the two 8.4 m mirrors of the LBT (Hill et al. 2006). The observations were carried out over five nights in 2017 March, in clear weather or thin clouds, with seeing $0\farcs6$–$1\farcs0$. We used a pixel scale of $0\farcs25$, the 210 grating in *H*-band and a slit width of $1\farcs0$, yielding a spectral resolution of $R \sim 3000$. We adopted a two-point dithering pattern and an exposure time of 5 minutes per frame, for a total on-source time of 21 hr (summed from both spectrographs). To facilitate acquisition, we used a multi-object mask and chose PA = 20° to align the slit to the major axis of the galaxy (Section 2.1). The data were reduced using the `flame` pipeline (Belli et al. 2017), which outputs a rectified, sky-subtracted, wavelength-calibrated two-dimensional (2D) spectrum. The corresponding Hα PV diagram is shown in Figure 1 (right, color scale).

2.4. One-dimensional Kinematic Profiles

To create the one-dimensional (1D) velocity and dispersion profiles in CO, we proceed as described by Genzel et al. (2017): we first fit a Gaussian profile to the CO line emission in each spaxel of the data cube, smoothed over three spaxels to ensure sufficient signal-to-noise ratio (S/N) in the outer parts of the galaxy. Accounting for the galaxy's systemic velocity, this results in the 2D velocity map. From this we determine $\mathrm{PA}_{\mathrm{kin}} = 23°$ as the axis with the steepest velocity gradient. It agrees with PA_H, and with the PA of the Hα slit observations (Sections 2.1, 2.3). The CO 1D velocity and dispersion profiles are then constructed from $0\farcs75$ diameter apertures (as a

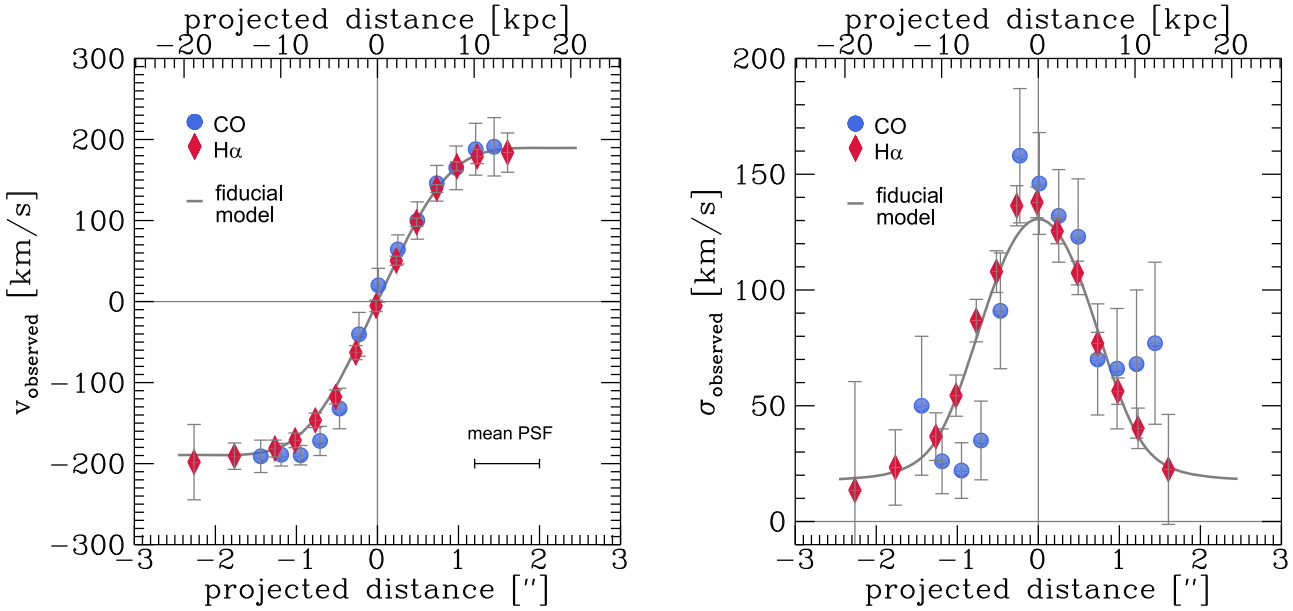

Figure 2. One-dimensional velocity (left) and velocity dispersion (right) profiles along the kinematic major axis in CO(3–2) (blue circles) and Hα (red diamonds). Due to the spatial resolution of the observations, neighboring data points are not independent. The projected distance increases from NE to SW of the kinematic center of the galaxy. The extractions from the two tracers agree. In gray we show our fiducial model (see Section 4.1).

compromise between the CO data resolution and the seeing-limited Hα data) with the center spaced by 0.″24 along PA_{kin}.

To create the 1D profiles in Hα, we extract spectra in overlapping bins of two to four spatial pixels and fit a Gaussian profile to the Hα line emission. The choice of the number of spatial pixels used for the extraction of individual data points does not substantially affect the extracted values, but allows for increased S/N in the outer disk regions.

We trace Hα out to 19 kpc (NE, ∼4.4 $R_{e,H}$) and 13 kpc (SW, ∼3.1 $R_{e,H}$), and CO out to 12 kpc (∼2.8 $R_{e,H}$). These physical radii at $z \sim 1.4$ are equivalent to probing the rotation curve out to 23–35 kpc for a galaxy of this stellar mass at $z \sim 0$ (van der Wel et al. 2014). Figure 2 shows the 1D velocity and dispersion profiles in CO and Hα along PA_{kin} in observed space. The uncertainties are derived from the Gaussian fits described above where noise has been taken into account. The two tracers agree, indicating that they trace the same mass distribution, most reliably in the outer disk where beam-smearing effects become less important.

The galaxy's intrinsic velocity dispersion, ∼15–30 km s^{-1}, is at the lower end of typical values of SFGs at this redshift (∼45 km s^{-1}; Wisnioski et al. 2015; see also Di Teodoro et al. 2016). This is evident from the outer regions of the 1D profile, where, under the assumption of constant intrinsic velocity dispersion, the effect of beam-smearing on the measured dispersion is low. Therefore, in the case of EGS4-24985, the correction for pressure support from the turbulent gas motions to the circular velocity is small (∼8 km s^{-1} at 2.″3), and thus does not lead to a significant drop in the observed outer rotation curve. Considering the limitations of the instrumental spectral resolution, the recovered dispersion values represent upper limits.

3. Modeling

Because the 1D kinematic profiles of ionized and molecular gas agree within their uncertainties, it is justified to combine them in order to improve constraints on our model parameters. We have also separately analyzed the Hα and CO data and found agreement of the results within the uncertainties (Table 1).

The kinematic modeling of our galaxy follows the methodology described by Wuyts et al. (2016) and Genzel et al. (2017). We build a mass model consisting of a thick exponential disk ($n_S = 1$, $q_0 = 0.2$), a bulge ($n_S = 4$, $q_0 = 1$, $R_e = 1$ kpc), and an NFW halo. We fit the mass model simultaneously to the 1D velocity and dispersion profiles of Hα+CO along PA_{kin}. For the baryonic mass distribution, we account for a finite flattening following Noordermeer (2008). Our choice of an $n_S = 1$ disk plus bulge is motivated by the bulge-to-disk decomposition and the likely high dust obscuration in the center of the galaxy.

The modeling uses an updated version of DYSMAL (Cresci et al. 2009; Davies et al. 2011; Wuyts et al. 2016). This code accounts for spectral and spatial beam-smearing, and incorporates the effects of pressure support on the circular velocity from the turbulent gas motions of the kinematic tracer, as described by Burkert et al. (2010) and Wuyts et al. (2016; see also Dalcanton & Stilp 2010 for a detailed discussion). The most important update to DYSMAL consists of the implementation of an MCMC sampling procedure using the EMCEE package (Foreman-Mackey et al. 2013). A full description of the updated code will be presented by T. T. Shimizu et al. (2018, in preparation).

Free parameters in our modeling are M_{bar}, R_e, B/T, i, σ_0, and the NFW halo mass M_{halo}. We choose the prior halo mass to be typical for the redshift and stellar mass of our galaxy (Moster et al. 2013). The concentration parameter is fixed to a value typical for this halo mass and redshift, $c = 4.4$ (Dutton & Macciò 2014). We verify that the typical concentration parameters for the range of halo masses derived from the MCMC sampling are broadly consistent with this value ($\Delta c \sim 0.2$ for the 1σ distribution of sampled halo masses). We explore setups with lower/higher concentrations ($c = 2$; 8), and consequently find lower/higher $f_{DM}(\leqslant R_e)$ and higher/

Table 1
Results from Our Fiducial Model and Additional Setups

Model	Fiducial Hα+CO	Only Hα	Only CO	Low c Hα+CO	High c Hα+CO	Free Halo, B/T Hα+CO	2 Fixed Disks Hα+CO
$M_{\rm bar}$ [$10^{11} M_\odot$]	G(1.4; 0.7) $1.1^{+0.5}_{-0.4}$	G(1.4; 0.7) $1.1^{+0.5}_{-0.3}$	G(1.4; 0.7) $1.2^{+0.5}_{-0.4}$	G(1.4; 0.7) $1.2^{+0.4}_{-0.3}$	G(1.4; 0.7) $1.2^{+0.5}_{-0.4}$	G(1.4; 0.7) $1.0^{+0.5}_{-0.4}$	f: 0.74 + 0.69 …
R_e [″]	G(0.52; 0.10) $0.49^{+0.10}_{-0.09}$	G(0.52; 0.10) $0.51^{+0.10}_{-0.10}$	G(0.52; 0.10) $0.50^{+0.10}_{-0.09}$	G(0.52; 0.10) $0.53^{+0.09}_{-0.08}$	G(0.52; 0.10) $0.48^{+0.11}_{-0.10}$	G(0.52; 0.10) $0.50^{+0.10}_{-0.10}$	f: 0.52; 0.26 …
B/T	G(0.20; 0.15) $0.27^{+0.10}_{-0.09}$	G(0.20; 0.15) $0.28^{+0.10}_{-0.09}$	G(0.20; 0.15) $0.22^{+0.12}_{-0.11}$	G(0.20; 0.15) $0.23^{+0.08}_{-0.07}$	G(0.20; 0.15) $0.29^{+0.11}_{-0.10}$	F[0;1] $0.43^{+0.28}_{-0.18}$	… …
i [°]	G(55; 10) 44^{+8}_{-6}	G(55; 10) 44^{+9}_{-7}	G(55; 10) 47^{+9}_{-7}	G(55; 10) 50^{+8}_{-7}	G(55; 10) 39^{+9}_{-6}	G(55; 10) 40^{+11}_{-9}	f: 55 …
σ_0 [km s^{-1}]	G(30; 10) 17^{+5}_{-6}	G(30; 10) 21^{+5}_{-6}	G(30; 10) 19^{+7}_{-7}	G(30; 10) 16^{+5}_{-6}	G(30; 10) 18^{+5}_{-6}	G(30; 10) 17^{+5}_{-6}	F[5;100] 11^{+7}_{-4}
$M_{\rm halo}$ [$10^{12} M_\odot$]	G(4.2; 2.0) $3.5^{+1.9}_{-1.7}$	G(4.2; 2.0) $3.5^{+1.9}_{-1.7}$	G(4.2; 2.0) $3.9^{+1.9}_{-1.8}$	G(4.2; 2.0) $4.4^{+1.9}_{-1.9}$	G(4.2; 2.0) $2.2^{+1.9}_{-1.3}$	F[0.001;100] $7.2^{+21}_{-5.1}$	F[0.01;100] $0.015^{+0.011}_{-0.004}$
c	f: 4.4 …	f: 4.4 …	f: 4.4 …	f: 2 …	f: 8 …	f: 4.4 …	F[1;10] $1.3^{+0.5}_{-0.2}$
inferred $f_{\rm DM}(\leqslant R_e)$	$0.18^{+0.06}_{-0.04}$	$0.19^{+0.06}_{-0.05}$	$0.20^{+0.08}_{-0.06}$	$0.11^{+0.04}_{-0.03}$	$0.25^{+0.07}_{-0.06}$	$0.22^{+0.08}_{-0.06}$	$0.008^{+0.002}_{-0.002}$

Note. We first list the model priors ("G(*x, y*)": Gaussian (center *x*, width *y*); "F[*x; y*]": flat prior in range [*x; y*]; "f: *x*": fixed to *x*) and then the medians with 1σ confidence ranges of the marginalized probability distributions from the MCMC sampling.

lower $M_{\rm halo}$, consistent with our main results (Table 1). We do not consider adiabatic contraction because its net effect at high redshifts is not well constrained (e.g., Duffy et al. 2010).

In calculating the model likelihood, we assume Gaussian measurement noise. For the purpose of parameter inference, we choose Gaussian priors for all model parameters that reflect our prior state of knowledge about their values and uncertainties (Table 1). As discussed in Section 2.1, q and R_e are independently constrained through GALFIT models. The adopted uncertainties of $\sigma_i = 10°$ and $\sigma_{R_e} = 0\farcs10$ are conservative estimates (see van der Wel et al. 2012). Through our choice of narrow Gaussian priors for these parameters, we translate their uncertainties directly into the modeling. We choose $B/T = 0.2$ with $\sigma_{B/T} = 0.15$ to account for a possible bulge hidden by dust extinction. For $M_{\rm bar}$ and $M_{\rm halo}$, we adopt uncertainties of ∼50%. For σ_0, our estimate is roughly based on the outer values of the dispersion profile. If we adopt flat priors for $M_{\rm halo}$ and B/T, we find consistent results. We also explored a model with fixed stellar and gaseous exponential disks, no bulge, free σ_0, $M_{\rm halo}$, and c, leading to a central dark matter fraction of <1% (Table 1).

For our fiducial model, we set up the MCMC sampling of the posterior probability function of the parameters with 180 walkers, a burn-in phase of 500 steps, and a running phase of 2000 steps. The length of the burn-in was designed to ensure convergence of the chains, while the length of the final run was designed to be >10 times the maximum autocorrelation time of the individual parameters. The acceptance fraction of the final run was 0.35.

4. Results

4.1. Parameter Correlations and Fiducial Model

The MCMC sampling of the joint posterior probability distributions of the model parameters is visualized in the top rows of Figure 3. The median values and 1σ confidence ranges of the marginalized distributions are indicated by the dashed vertical lines in the 1D histograms (see also the second column in Table 1).

For the 2D marginalized distributions, contours show the 1σ, 2σ, and 3σ confidence levels. The strongest correlation is between inclination and $M_{\rm bar}$. This is expected, since any inclination correction to the observed rotation velocity directly affects the inferred dynamical mass. This is also reflected to a smaller extent in the correlation between inclination and $M_{\rm halo}$.

Because the posterior distribution is well behaved, we choose our fiducial model to be represented by the median values of the individual marginalized distributions, with uncertainties represented by the 1σ confidence ranges. The median values are also shown as blue squares in the 2D histograms in Figure 3. Every median lies close to the mode of the posterior distribution in projection, indicating that they lie in the most likely parameter space.

The 1D profiles of velocity and dispersion corresponding to the fiducial model in observed space are shown as gray lines in Figure 2.

4.2. Central Dark Matter Fraction

We measure the enclosed dark matter fraction at R_e from the intrinsic properties of the DYSMAL model defined by the median sampling results, and find $f_{\rm DM}(\leqslant R_e = 0\farcs49) = v^2_{\rm DM}(R_e)/v^2_{\rm circ}(R_e) = 0.20$. $v_{\rm DM}$ is the contribution to the circular velocity of the dark matter halo, and $v_{\rm circ}$ is the total circular velocity. The galaxy is strongly baryon-dominated within R_e. This baryon-dominance prevails out to $r = 1\farcs46$ ($3\,R_e$). Our model agrees with the baryonic disk being "maximal," $v_{\rm disk}(R_{\rm max})/v_{\rm circ}(R_{\rm max}) = 0.90$, where $R_{\rm max} = 0\farcs44$ is the radius where the disk velocity reaches its peak value (e.g., van Albada et al. 1985). The intrinsic model rotation curve and mass component curves are shown in Figure 4. The inferred baryon-to-total mass fraction $m_d = 0.03$ is compatible with predictions from abundance matching estimates that account for gas mass (Burkert et al. 2016).

Through the MCMC sampling, we also gather information on the probability distribution of $f_{\rm DM}(\leqslant R_e)$, which is not itself a model parameter but is instead calculated from the intrinsic models. In Figure 3 (bottom row) we show the 1D and 2D

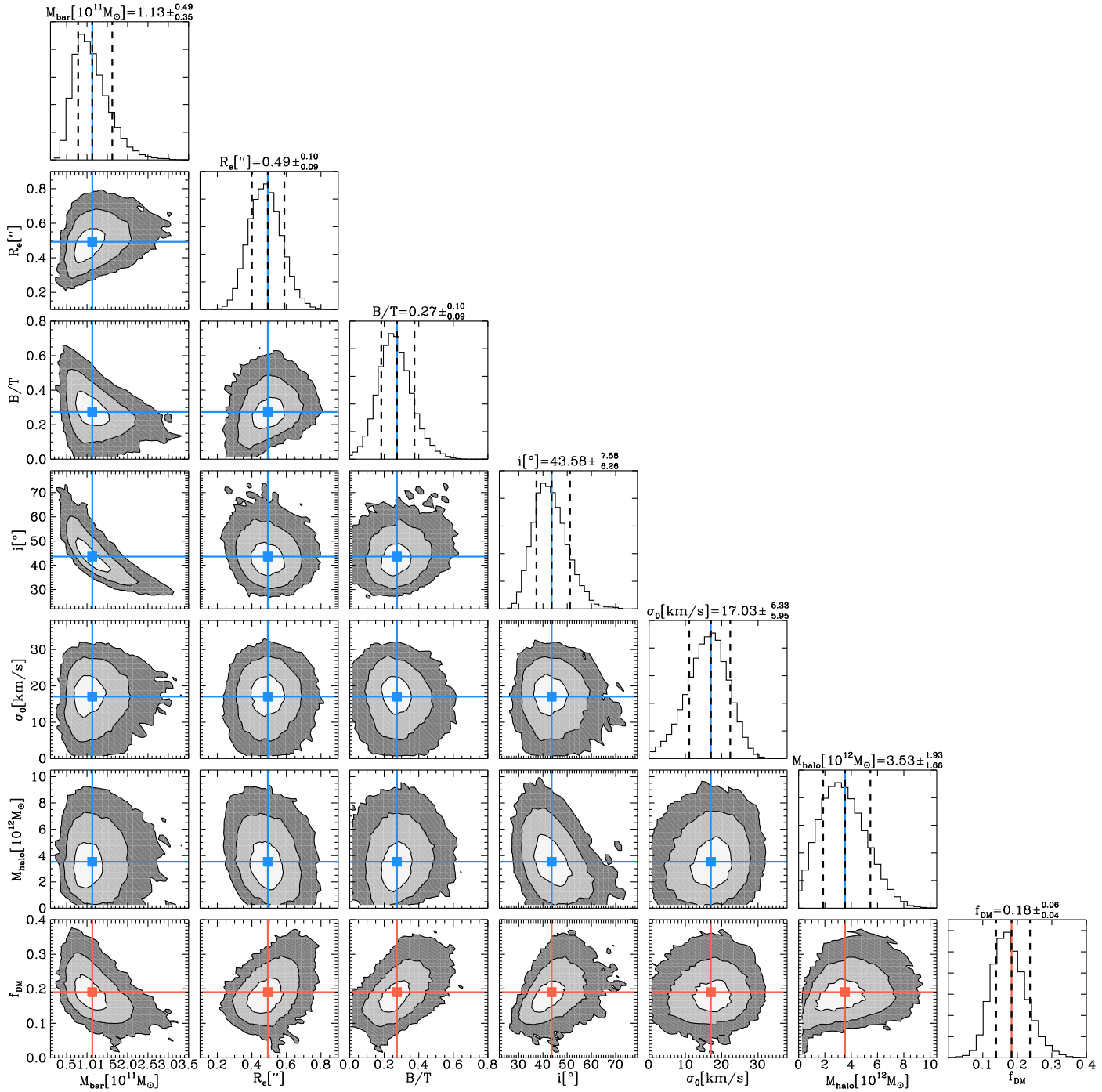

Figure 3. MCMC sampling of the joint posterior probability distribution of the fiducial model parameters, $M_{\rm bar}$, R_e, B/T, i, σ_0, and $M_{\rm halo}$ (top rows) from a combined fitting to the Hα+CO data. The median values and 1σ confidence ranges of the marginalized distributions are indicated by the dashed vertical lines in the 1D histograms, and given on top of each histogram. The median values are also shown as blue squares on top of the 2D histograms. All of the median values lie close to the modes of the 2D histograms. The contours show the 1σ, 2σ, 3σ confidence levels of the 2D distributions. The bottom row histograms show $f_{\rm DM}(\leqslant R_e)$, calculated from the intrinsic models. Median values are indicated in red. For the sampled parameter space, dark matter is sub-dominant within R_e.

histograms of the marginalized posterior distribution of the $f_{\rm DM}(\leqslant R_e)$ values associated with the sampled parameter space. While correlations with some of the model parameters are evident, particularly with $M_{\rm bar}$ and with the structural parameters R_e and B/T, dark matter is sub-dominant within R_e for the explored parameter space. We use the median and 1σ confidence ranges of the marginalized probability distribution to estimate $f_{\rm DM}(\leqslant R_e)$ and its uncertainties, and find $f_{\rm DM}(\leqslant R_e) = 0.18^{+0.06}_{-0.04}$.

5. Discussion and Conclusions

We have presented kinematic data of a $z = 1.4$ SFG based on independent and deep Hα and CO(3–2) observations. We find that the ionized and molecular gas trace the same gravitational potential, as their kinematics agree within the uncertainties. Thus, we combine them to model the galaxy.

We use MCMC sampling to constrain a mass model consisting of a thick exponential disk, a bulge, and an NFW halo. We find that the galaxy's central region is baryon-dominated with a dark

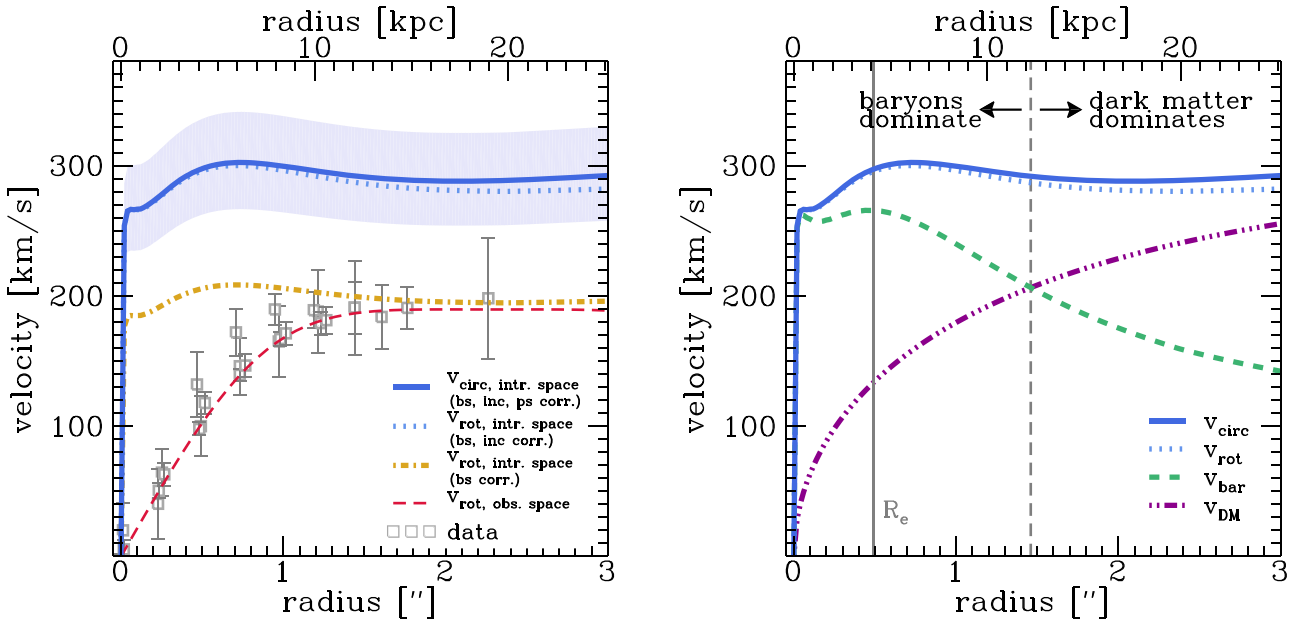

Figure 4. Left: rotation curve in observed vs. intrinsic space. The gray squares show the folded, observed velocity (Hα+CO) as a function of projected distance from the center. The red dashed line is our fiducial model in observed space. The dashed–dotted yellow line shows the model rotation velocity in observed space, corrected for beam-smearing ("bs"). The dotted blue line shows the intrinsic model rotation velocity, further corrected for inclination ("inc"). The solid blue line shows the intrinsic model circular velocity, further corrected for pressure support ("ps"), and the shaded area shows the 1σ uncertainties of the inclination correction. Right: intrinsic rotation curve of the fiducial model. The solid and dotted blue lines are as in the left panel. The baryonic contribution by the bulge and disk is shown as a dashed green line, and the dark matter contribution as a dashed–dotted purple line. The inner solid and the outer dashed vertical gray lines respectively show R_e, and the radius where baryons and dark matter contribute equally to the potential.

matter fraction of $f_{\rm DM}(\leqslant R_e) = 0.18^{+0.06}_{-0.04}$. This is in agreement with recent findings of low central dark matter fractions in high-redshift SFGs by several groups (Förster Schreiber et al. 2009; van Dokkum et al. 2015; Alcorn et al. 2016; Price et al. 2016; Stott et al. 2016; Wuyts et al. 2016; Genzel et al. 2017; Lang et al. 2017).

Together with $v_{\rm circ}(R_e) = 296\,{\rm km\,s^{-1}}$, this places EGS4-24985 into the same region of the $v_{\rm circ}$–$f_{\rm DM}$ parameter space as the two $z \sim 1.5$–1.6 galaxies observed in Hα by Genzel et al. (2017)—a region also populated by massive local SFGs (e.g., Persic & Salucci 1988; Begeman et al. 1991; de Blok et al. 2008; Lelli et al. 2016) and early-type galaxies (e.g., Cappellari et al. 2013). The latter are the likely descendants of massive SFGs at $z \sim 1$–3. Our result supports the interpretation by Genzel et al. (2017) that the low central dark matter fractions observed during the peak epoch of cosmic star formation rate density might be preserved over the rest of cosmic history, as massive SFGs quench and evolve into passive galaxies. Also, this suggests that massive disks are baryon-dominated in their centers at all times.

The low pressure support in our galaxy results in a flat intrinsic rotation curve despite the low $f_{\rm DM}(\leqslant R_e)$, thus setting it apart from the galaxies presented by Genzel et al. (2017). It also implies that, in this case, the slope of the rotation curve in the outer disk region is a closer tracer of the relative contributions of baryons and dark matter to the rotational support of the galaxy. The low intrinsic dispersion further suggests that the galaxy is more settled than other galaxies at this redshift with otherwise comparable physical properties (Genzel et al. 2017), indicating that any potential dissipative condensation has happened at earlier times (e.g., Dekel & Burkert 2014). Still, EGS4-24985 falls on the high-redshift Tully–Fisher relations (Übler et al. 2017).

The agreement of the deep Hα and CO data, especially in the outer disk, helps to alleviate concerns that ionized gas kinematics at high redshift might be unrepresentative of the galaxy kinematics, and could instead be circumgalactic or in-/outflowing gas in disguise. Future studies with high-quality resolved kinematics traced through multiple gas phases in SFGs at similar redshifts will be important to statistically corroborate our result.

We are grateful to the anonymous referee for a constructive report that helped to improve this manuscript. We thank the staff at IRAM and LBT for their helpful support with the NOEMA and LUCI observations for this work.

ORCID iDs

H. Übler https://orcid.org/0000-0003-4891-0794
R. Genzel https://orcid.org/0000-0002-2767-9653
L. J. Tacconi https://orcid.org/0000-0002-1485-9401
N. M. Förster Schreiber https://orcid.org/0000-0003-4264-3381
R. Neri https://orcid.org/0000-0002-7176-4046
S. Belli https://orcid.org/0000-0002-5615-6018
E. J. Nelson https://orcid.org/0000-0002-7524-374X
P. Lang https://orcid.org/0000-0002-5681-3575
T. T. Shimizu https://orcid.org/0000-0002-2125-4670
R. Herrera-Camus https://orcid.org/0000-0002-2775-0595
S. H. Price https://orcid.org/0000-0002-0108-4176
K. Tadaki https://orcid.org/0000-0001-9728-8909
E. Wisnioski https://orcid.org/0000-0003-1657-7878
S. Wuyts https://orcid.org/0000-0003-3735-1931

References

Alcorn, L. Y., Tran, K.-V. H., Kacprzak, G. G., et al. 2016, ApJL, 825, L2
Begeman, K. G., Broeils, A. H., & Sanders, R. H. 1991, MNRAS, 249, 523

Belli, S., Contursi, A., & Davies, R. I. 2017, arXiv:1710.05924
Burkert, A., Förster Schreiber, N. M., Genzel, R., et al. 2016, ApJ, 826, 214
Burkert, A., Genzel, R., Bouché, N., et al. 2010, ApJ, 725, 2324
Buschkamp, P., Seifert, W., Polsterer, K., et al. 2012, Proc. SPIE, 8446, 84465L
Cappellari, M., Scott, N., Alatalo, K., et al. 2013, MNRAS, 432, 1709
Chabrier, G. 2003, PASP, 115, 763
Chen, C.-C., Hodge, J. A., Smail, I., et al. 2017, ApJ, 846, 108
Cresci, G., Hicks, E. K. S., Genzel, R., et al. 2009, ApJ, 697, 115
Dalcanton, J. J., & Stilp, A. M. 2010, ApJ, 721, 547
Davies, R., Förster Schreiber, N. M., Cresci, G., et al. 2011, ApJ, 741, 69
de Blok, W. J. G., Walter, F., Brinks, E., et al. 2008, AJ, 136, 2648
Dekel, A., & Burkert, A. 2014, MNRAS, 438, 1870
Di Teodoro, E. M., Fraternali, F., & Miller, S. H. 2016, A&A, 594, A77
Duffy, A. R., Schaye, J., Kay, S. T., et al. 2010, MNRAS, 405, 2161
Dutton, A. A., & Macciò, A. V. 2014, MNRAS, 441, 3359
Foreman-Mackey, D., Hogg, D. W., Lang, D., & Goodman, J. 2013, PASP, 125, 306
Förster Schreiber, N. M., Genzel, R., Bouché, N., et al. 2009, ApJ, 706, 1364
Genzel, R., Förster Schreiber, N. M., Übler, H., et al. 2017, Natur, 543, 397
Genzel, R., Tacconi, L. J., Kurk, J., et al. 2013, ApJ, 773, 68
Genzel, R., Tacconi, L. J., Lutz, D., et al. 2015, ApJ, 800, 20
Grogin, N. A., Kocevski, D. D., Faber, S. M., et al. 2011, ApJS, 197, 35
Hill, J. M., Green, R. F., & Slagle, J. H. 2006, Proc. SPIE, 6267, 62670Y
Koekemoer, A. M., Faber, S. M., Ferguson, H. C., et al. 2011, ApJS, 197, 36
Kriek, M., Shapley, A. E., Reddy, N. A., et al. 2015, ApJS, 218, 15
Lang, P., Förster Schreiber, N. M., Genzel, R., et al. 2017, ApJ, 840, 92
Lang, P., Wuyts, S., Somerville, R. S., et al. 2014, ApJ, 788, 11
Lelli, F., McGaugh, S. S., & Schombert, J. M. 2016, AJ, 152, 157
Moster, B. P., Naab, T., & White, S. D. M. 2013, MNRAS, 428, 3121
Navarro, J. F., Frenk, C. S., & White, S. D. M. 1996, ApJ, 462, 563
Noordermeer, E. 2008, MNRAS, 385, 1359
Olivares, V., Treister, E., Privon, G. C., et al. 2016, ApJ, 827, 57
Peng, C. Y., Ho, L. C., Impey, C. D., & Rix, H.-W. 2010, AJ, 139, 2097
Persic, M., & Salucci, P. 1988, MNRAS, 234, 131
Price, S. H., Kriek, M., Shapley, A. E., et al. 2016, ApJ, 819, 80
Skelton, R. E., Whitaker, K. E., Momcheva, I. G., et al. 2014, ApJS, 214, 24
Stott, J. P., Swinbank, A. M., Johnson, H. L., et al. 2016, MNRAS, 457, 1888
Swinbank, A. M., Papadopoulos, P. P., Cox, P., et al. 2011, ApJ, 742, 11
Tacconi, L. J., Genzel, R., Saintonge, A., et al. 2018, ApJ, 853, 179
Turner, O. J., Cirasuolo, M., Harrison, C. M., et al. 2017, MNRAS, 471, 1280
Übler, H., Förster Schreiber, N. M., Genzel, R., et al. 2017, ApJ, 842, 121
van Albada, T. S., Bahcall, J. N., Begeman, K., & Sancisi, R. 1985, ApJ, 295, 305
van der Wel, A., Bell, E. F., Häussler, B., et al. 2012, ApJS, 203, 24
van der Wel, A., Franx, M., van Dokkum, P. G., et al. 2014, ApJ, 788, 28
van Dokkum, P. G., Nelson, E. J., Franx, M., et al. 2015, ApJ, 813, 23
Whitaker, K. E., Franx, M., Leja, J., et al. 2014, ApJ, 795, 104
Wisnioski, E., Förster Schreiber, N. M., Wuyts, S., et al. 2015, ApJ, 799, 209
Wuyts, S., Förster Schreiber, N. M., Lutz, D., et al. 2011, ApJ, 738, 106
Wuyts, S., Förster Schreiber, N. M., Wisnioski, E., et al. 2016, ApJ, 831, 149